Title: Sea floor bedforms and their influence on slope accommodation.

Authors: Maselli, V.[1,2], Kneller, B. [1], Taiwo, O.L. [1], Iacopini, D. [1]

[1]School of Geosciences, University of Aberdeen, Meston Bld., King's College, Aberdeen, AB24 3UF, United Kingdom.

[2]Department of Earth Sciences, Life Sciences Centre, Dalhousie University, 1355 Oxford Street, Halifax, Nova Scotia, B3H 4R2, Canada.

Keywords: Stoss accommodation space, intra-slope basin, turbidity currents, bedforms, offshore Brazil.

Highlights:

1- 3D seismic data are used to investigate sea floor morphology and underneath stratigraphy in the Potiguar Basin, offshore Brazil.

2- Large- and short-wavelength bedforms are recognized.

3- Ponded lobes accumulate on the stoss side of the large-wavelength bedforms, and seismic attributes are used to characterize the associated lithology.

4- The concept of stoss accommodation space is introduced.

Abstract

In deep-water settings, the accommodation space for sediment transported by turbidity flows relates to the difference between the elevation of the depositional surface and its equilibrium profile. As a consequence, accommodation space creation, or disruption, may depend from

changes in the physiography of the receiving basin, or changes in the flow properties. In topographically complex slopes, such where salt-withdrawal intra-slope basins occur, three different types of accommodation space have been recognized. Among other parameters, the ratio between flow thickness and depth of the intra-slope basin controls the partial, or full, ponding of the sediment in suspension, and consequently, the lithology distribution within the deposit. On a smaller spatial scale, the behavior of turbidity flows is affected by the topography of the sea floor. Indeed, the presence of large-wavelength bedforms may generate local topographic low compared to the adjacent sea floor that may trap part of the sediment carried by sediment-laden flows, such as turbidity flows or bottom currents.

With a beautiful example from the offshore Brazil, we show how ponded lobes accumulate on the convex-up stoss side of pre-existing sea floor bedforms and how the three-dimensional topography of the sea floor controls the flow behavior and the deposition farther downslope. In detail, using 3D seismic data and attributes we demonstrate that the stoss side of the bedform traps the coarse-grained fraction of turbidity currents flowing downslope, while the fine-grained cloud spills over its crest. Further studies are necessary to fully understand the behavior of sediment-laden flows on a complex sea floor topography, the preservation potential of such deposits and the role of *stoss accommodation* in the evolution of deep-water depositional systems.

1. Introduction

Accommodation space was defined by Vail (1987) and Jervey (1988) as the space available for sediment accumulation, with global sea level change and tectonic processes (driving subsidence or uplift of the sea floor) considered as first order controls. In shallow water shelfal systems, the accommodation space available is also dependent from the energy of

marine processes, such as waves, longshore drift or tides, and by the presence of topographic lows, such as incised valleys (Dalrymple et al., 1992).

In deep-water settings, the concept of accommodation space was expanded considering the analogy between subaerial (rivers) and submarine channels, both characterized by downstream concave-up equilibrium profiles and a base level (Carter, 1988; Prather et al., 1998; Pirmez et al., 2000; Kneller, 2003). A topographic profile is considered in equilibrium, or at grade, when the kinetic energy distribution along the system is such that no net sediment aggradation or erosion occurs. In fluvio-deltaic systems the base level coincides with sea or lake levels, i.e. the channel mouth, while for submarine channels the base level was defined as the deepest point reached by a gravity-driven flow (Carter, 1988), or the point where the transition from confined to unconfined flow occurs (Kneller, 2003). Turbidity currents exert a paramount control on the shape of the equilibrium profile with the gradient of submarine channels directly related to the flow conditions (flow density, thickness, grain size, mud content; Mutti et al., 1999; Kneller, 2003). Considering the above, the accommodation space was defined by the difference between the topography of the depositional surface (i.e., the thalweg of a slope turbidite channel) and its equilibrium profile (Prather et al., 1998; Pirmez et al., 2000). When a submarine channel is at grade, the accommodation space is limited, a meandering planform morphology develops, with no aggradation or incision (Kneller, 2003), producing fluvial-like meander belts (Abreu et al., 2003; Kolla et al., 2012).

A disequilibrium between the channel thalweg and the graded profile will lead to accommodation space creation or destruction that the system will exploit through deposition within the channel or erosion of its thalweg and rejuvenation of the system (Pirmez et al., 2000; Heiniö and Davies, 2007). Several mechanisms, mainly driven by tectonic processes (Prather et al., 1998; Pirmez et al., 2000; Ferry et al., 2005) or emplacement of mass-transport deposits (Armitage et al., 2009; Kneller et al., 2016 and references therein), may lead to the

formation of accommodation space for sediment deposition. The topography of the slope may change in response to shale or salt diapirism under loading by thick sediment accumulations, or in response to gravitational tectonics driven by rapid sedimentation along passive margins (Prather, 2003), or by crustal extension or compression, leading to the formation of ponded and healed-slope accommodation space (*sensu* Prather et al., 1998). Ponded slope basins have been recognized in different settings, both modern and ancient, and extensively investigated in the Gulf of Mexico and in the Eastern Equatorial Atlantic margin (Prather et al., 1998; Beaubouef and Friedmann, 2000; Pirmez et al., 2000; Sinclair and Tomasso, 2002; Booth et al., 2003; Smith, 2004; Barton, 2012; Deptuck et al., 2012; Prather et al., 2012; Jobe et al., 2015; Jobe et al., 2017; Hawie et al., 2018). Through integration of seismic and well data, the motif of the sedimentary infill has been interpreted in terms of a process of fill-and-spill, i.e filling of the mini-basin by ponded turbidites and associated deposits, and subsequent bypass from the shallower mini-basin to the one downslope (Winker, 1996; Prather et al., 1998; Badalini et al., 2000; Prather et al., 2012). Mass-transport deposits (MTDs), ubiquitously recognized in all margin settings, have the potential to generate different styles of accommodation space and to control deep-water sediment routing systems (Kneller et al., 2016; Soutter et al., 2018). Sediment may accumulate along the evacuation zone of submarine landslides or along the relative topographic lows generated atop the MTDs by the presence of blocks, faults, folds and compaction (Kneller et al., 2016).

Local topographic changes of the sea floor (i.e., bedforms) have been observed on the slope in association with the passage of gravity-driven flows such as turbidity currents, or of bottom currents (Wynn and Stow, 2002; Smith et al., 2007; Piper and Normark, 2009; Rebesco et al., 2014; Talling et al., 2015; Symons et al., 2016 and references therein). Turbidity and bottom currents interacting with the sea floor may generate bedforms both depositional (sediment waves), erosional (scours), or mixed, generated where both erosion

and deposition occurs (terminology *sensu* Symons et al., 2016). Bedforms of different shapes, aspect ratio, direction of migration and grain size, from mud to gravel, have been recognized in both confined and unconfined settings, such as shelfal systems (Berndt et al., 2006), pro-delta slopes (Casalbore et al., 2017), channel axis (Paull et al., 2010; 2011), channel levees (Normark et al., 2002), and channel-lobe transitions (Carvajal et al., 2017). After the seminal work of Fildani et al. (2006) on the Monterey East Channel, increasing attention has been dedicated to the study of bedforms, including those described as cyclic steps and their associated supercritical flow regimes (i.e., densimetric Froude numbers >1). Cyclic steps and antidunes have been increasingly recognized along delta fronts (Normandeau et al., 2016; Hughes Clarke, 2016) and slope channel systems (Covault et al., 2017), and a growing body of evidence has suggested that channels may evolve from a series of erosional bedforms arranged in a cyclic manner (i.e., cyclic steps; Fildani et al., 2013; Covault et al., 2014). On the sea floor, erosional bedforms, or those with an erosional component, may reach up to 10^3 m in length and width, and up to 10^2 m in height (Cartigny et al., 2011; Symons et al., 2016), often showing circular to elliptical morphology, such as in the case of the Monterey East channel (Fildani et al., 2006). With respect to the adjacent sea floor, the stoss side of such bedforms constitutes an area of lower bathymetry, and consequently represent accommodation space for sediment accumulation.

This study aims to understand the role of topographic lows generated by turbidity-current-related bedforms (both erosional and depositional) in promoting slope accommodation space and affecting sediment dispersal patterns and pathways. Using an example from the Brazilian slope in the offshore Potiguar basin, we will demonstrate how the stoss side of large-wavelength bedforms may act as a mini-basin where coarse-grained sediments transported by turbidity currents may accumulate generating ponded lobes. Moreover, we will discuss how the flow transformation of turbidity currents through flow stripping across the bedform-

related ponded mini-basin may affect the sedimentation pathways and related sea floor topography of the slope farther downslope.

2. Study Area and Geological Setting

The present study focuses on a portion of the Brazilian slope just south of the Equator, in the offshore Potiguar basin, in water depths between ca. 700 m and 1800 meters below mean sea level (m bmsl; Fig. 1). The area is characterized by a ca. 60 km wide, low angle (0.04°), shelf, and a steep slope, dipping towards NE at ca. 3.8°. Towards the basin, in deeper water, a series of volcanic islands and structural highs develop, creating troughs that interrupt the continuity of the slope (Fig. 1).

The Potiguar basin is a NE-trending aborted rift with ~6,000 m thick sedimentary infill, structurally characterized by SW-NE-trending asymmetric grabens separated by internal basement horsts (Matos, 2000; Jovane et al., 2016). The rifting process began in response to continental breakup between the Borborema and Benin-Nigeria provinces during the South Atlantic opening in the Early Cretaceous (Matos, 2000). Rift phase deposition during the Aptian to Campanian, consisted of fluvial to shallow-marine transgressive sediments (Araripe and Feijó, 1994). The drift phase, starting in the Campanian, is characterized by thermal subsidence and deposition of fluvio-deltaic to deep-water clastic sediments, with the Neogene mainly recording the onset and evolution of the submarine canyon systems still active today.

3. Data and Methods

The dataset from the Potiguar Basin used in the present study consists of a high-quality 3D full stack, Kirchhoff time-migrated reflection seismic volume, covering about ~2000 km^2, and acquired by PGS in 2009 (Fig. 1). The line spacing is 12.5 m in both in-line and cross-

line directions. The sample interval is 2 milliseconds (ms). The data are zero-phase migrated and displayed with Society for Exploration Geologists (SEG) normal polarity, so that an increase in acoustic impedance is represented by a blue-red-blue reflection loop. The dominant frequency (F) of the section of interest (upper 250 ms below the seabed) ranges between 40 and 75 Hz. Sound velocities of 1,500 ms^{-1} and 1,800-2,500 ms^{-1} have been respectively assigned for sea water and for the investigated interval below the sea floor, with the latter velocity obtained from the sonic log of well CES-112, located 2 km to the SE (see Fig. 1; Conde et al., 2007). Using those end-member velocities and frequencies, we estimate a vertical resolution (defined as tuning thickness, or limit of separability, as $\lambda/4$, λ being the wavelength of the P wave) as 5 m at the sea floor and 6 to 15.5 m for the units below. Taking into account the focusing effect of Kirchhoff migration (Brown, 2004), a radius Fresnel zone (with a radius equal to velocity $V_{average}/4F$) of 5 m to 15.5 m can be reasonably expected, and therefore a minimum diameter 10-31 m represents the limit of our interpretation analysis on a horizon (*sensu* Brown, 2004). However our ability to recognize sea floor features in plan view, defined as detectability or limit of visibility (Brown, 2004), can go below the tuning thickness limit (Brown, 2004); while in the 3D migrated dataset, reflectors (e.g., peak to peak) will be at least 5 m thick, and two reflecting point in horizontal space need to be around 5-15 m a part, when we are mapping the seafloor as a surface horizon, geological features on considerably smaller scales can be detected and visualized with greater detail (Reijenstein et al., 2011). Thus we can describe geological and sedimentary features or patterns smaller than the tuning thickness, although our capacity to define volumes is limited by the tuning thickness.

The bathymetry of the sea floor, presented at a 12.50×12.5 m of horizontal resolution (Fig. 2), was generated picking the first reflection from the 3D seismic data. Two other seismic horizons, H1 and H2, were identified on 2D arbitrary lines extracted from the 3D seismic

volume, based on the seismic facies and reflector terminations. The structural map of each seismic horizon is presented as surface gridded at a 12.5 × 12.5 m of horizontal resolution.

Seismic attributes have been calculated and extracted from the sea floor horizon and include both amplitude-derived (root-mean-square, RMS) and time-derived (variance) values. While the variance, which measures the similarity of consecutive waveforms over a given sampling window (3 × 3 traces in the present study), is useful for imaging lateral discontinuities (Chen and Sidney, 1997; Brown, 2004), the RMS amplitude, which represents the square root of the arithmetic mean of the squares of the amplitudes within a defined window interval (3 instantaneous traces in the present study), is helpful for revealing coarse-grained facies (Rijks and Jauffred, 1991; Chen and Sidney, 1997; Brown, 2004).

4. Results

4.1. Sea floor morphology

The sea floor shows two main canyon-channel systems, named C-1 and C-3 (Fig. 2) that are located towards NW and SE corners of the dataset, respectively. The depth of both channels changes from ca. 400 m to less than 200 downslope, while the thalweg presents an average gradient of 2.7° and a sinuosity index of 1.158, for C-1, and a gradient of 3.8° and a sinuosity index of 1.028, for C-3 (Fig. 2). A smaller channel, C-2, ca. 90 m deep, crosses the slope with an average thalweg gradient of 4.15° and a sinuosity index of 1.031. The present study focuses in the slope area comprised between C-2 and C-3 (confined by the red line in Fig. 2).

Two narrow channel incisions (C-A and C-B, Fig. 2), up to 60 m deep and oriented SW-NE, form upstream of a topographic step (slope break) oriented approximately NS (dashed red line in Fig. 2). Farther downslope, the sea floor presents a series of large-wavelength bedforms (Fig. 3), named LB1 to LB4, which are clearly highlighted by the variance attribute

extracted from the sea floor horizon (Fig. 3 right, and Fig. 4). The bedform wavelength changes from ca. 4 km (LB1, Fig. 5) to less than 1 km (LB4, Fig. 5), while the bedform height from ca. 150 m (LB1, Fig. 5) to less than 50 m (LB4, Fig. 5). The crests of the bedforms show a sinuous shape, with dominant downslope convexity (Fig. 3), and are progressively shifted towards East moving downdip, following the maximum gradient of the sea floor.

In a cross section on the sea floor, the bedforms are downslope asymmetric, with seaward dipping (LB1 and LB2, Fig. 3 bottom) or sub-horizontal (LB3 and LB4) stoss sides, and up to 8° dipping lee sides. A series a small channels (named gutter-like channels), up to 15 m deep, incise the lee sides of LB1 to LB4, and the area farther downslope.

On the sea floor, the stoss side of LB1, just downdip of the slope break at the mouth of C-A and C-B, is characterized by two fields of short-wavelength bedforms (SB1a and SB1b, Fig. 3), both symmetric (section a-b in Fig. 6) and asymmetric (section c-d in Fig. 6), and with sinuous crests (Fig. 6, right). Wavelengths and heights are, on average, 120 m and 8 m, respectively (Fig. 5). A third train of bedforms (named SB2) with linear crests and ca. 5 m wave heights is present on the lee side of LB3 (SB2 in Fig. 3; section e-f in Fig. 6). We are confident that the spatial (vertical and horizontal) resolution of the sea floor generated by picking the sea floor horizon on the 3D seismic dataset is high enough to visualize such small-scale sea floor features. Seismic artefacts are present in the data, as indicated the contour-parallel undulations highlighted by the slope map of Fig. 6, but they are characterized by a totally different seismic footprint (see section g-h in Fig. 6), unrelated to the bathymetry, with wave height and length extremely short, which will not have any effect on the interpreted structures.

The RMS amplitude extraction map of the sea floor (Fig. 7) shows lobe-shaped areas characterized by high RMS values on the stoss side of each large-wavelength bedform

(highlighted in orange in the B/W version of the RMS map in Fig. 7C). In detail, high RMS values can be found where SB1a, SB1b and SB2 fields develop (named Lobe A, Lobe B and Lobe D, respectively, Figs. 6, 7), on the stoss side of LB2 (Lobe C, Figs. 6, 7), of LB4 (Lobe E, Figs. 6, 7), and of LB3 towards the northern flank of channel C-3 (Lobe F in Figs. 6, 7). High RMS amplitude values also characterize the southern flank of C-2, while low values can be detected along the lee side of all the large-wavelength bedforms (Fig. 7)

4.2. Seismic stratigraphy

The stratigraphy of the study area, and in particular of the lobe-shaped areas identified in the RMS attribute map (Fig. 7), has been revealed using a combination of 2D arbitrary lines extracted from the 3D seismic cube, surface maps of key stratigraphic horizons and thickness maps (Figs. 8, 9).

Horizon H1, identified by a continuous positive reflection, is the first continuous horizon below the sea floor, which can be traced in much of the study area (Figs. 8, 9B). The horizon forms at the base of a series of lobe-to-lens-shaped deposits (named Lobe A to Lobe F, in Figs. 7, 8, 9), whose tops correspond to the sea floor and show high RMS amplitude values. In the same position, corresponding to the stoss side of the large-wavelength bedforms (Figs. 3, 7), the surface map of H1 shows a series of topographic depressions, triangular to circular in shape, with progressively reducing size downslope (Fig. 9B). Thickness map of the unit between the sea floor and horizon H1 (Fig. 9D) shows a series of sediment depocenters up to 65 m thick (Lobe A, Fig. 9D), whose internal seismic character is highlighted in Figure 8 (Lobes A, B, D and F, as examples). Each lobe shows a positive relief respect to the adjacent sea floor, and is confined basinward by the topography generated by the large-wavelength bedforms (Fig. 8). Lobe A, in detail, is the largest sediment depocenter, covering a surface

area of ca. 3.5 km^2 (Fig. 9D), and is composed by thick, high-amplitude, and wavy reflections (seismic lines 1, 2 and 5 in Fig. 8). The sea floor reflection on top of Lobe A is also wavy (Fig. 8), and corresponds to the short-wavelength bedform field SB1a visible on the sea floor maps of Figures 3 and 6. Thickness map (Fig. 9D) highlights that Lobe A is made up of two bodies, with the shallower backstepping with respect to the deeper (see seismic line 5 in Fig. 8). Lobe A accumulates on the stoss side of the large-wavelength bedform LB1, which is confined by horizon H1 at its top and horizon H2 at its base (Figs. 8, 9E). Horizon H2 shows an erosional character, as highlighted by several truncated reflections (see the black arrows in Fig. 8), and can be traced over part of the study area (Fig. 9C). The topographic depression generated by H2 is exploited by the accumulation of LB1, which is a 90 m thick, L shaped, sediment body (Fig. 9E), made by continuous and low amplitude reflections, showing lateral (see seismic lines 3 and 4 in Fig. 8) and upslope (see seismic line 5 in Fig. 8) migration of progradation, and internal erosional surfaces (highlighted by black dashed lines in the seismic profiles of Fig. 8). The deposition of the large-wavelength bedform LB1 visible on the sea floor (Figs. 3, 4) creates the accommodation space for the accumulation of Lobe A and its downslope confinement, as shown by Figure 9F. Similar geometric relations are observed for each Lobe B to F, where the deposition of a lower unit bounded by an erosional surface (see the red dashed lines in seismic lines 6 and 7 in Fig. 8, and line 8 in Fig. 9) causes the generation of the large-wavelength bedforms and for the formation of accommodation space along the slope. RMS amplitude extraction of the sea floor integrated with the seismic facies in cross section highlight that each lobe has high RMS values and is made by high-amplitude reflections (Fig. 7). By contrast, the units beneath, which crop out on the seafloor along the lee side of the large-wavelength bedforms, present low RMS amplitude and mainly low amplitude seismic reflections (Figs. 7, 8, 9). Consequently, we can infer that the lobes are made by coarser-grained (probably sandy) sediment compared to the deposit beneath that are

responsible for the formation of the large-wavelength bedforms, which are probably muddier. Correlation of horizon H2 with the other erosional surfaces occurring farther downslope is not straightforward, which poses problem is the development of a conceptual model for explaining their evolution. In the supplementary material we present two models which take into account the effect of different processes and the possibility that the erosional surfaces occurred synchronously to H2, or not.

5. Discussion

Topographically complex slopes (*sensu* Smith, 2004) occur when tectonic processes or deformations of the sea floor driven by sediment loading on a mobile substrate crate topographic lows or highs that can affect the path and behavior of gravity-driven flows traveling downslope. In such contexts, different types of accommodation space may exist (namely ponded, healed and slope accommodation; Prather et al., 1998), whose infill reflects the effect of changing accommodation space through time (due to deposition), on the behavior of gravity flows, and on the instability of the slope (Prather, 2003). Accommodation space can be generated *a-priori*, and then filled by sediments, or can be increased by sediment loading during basin infill, as in the case of salt withdrawal intra-slope basins (Winker, 1996; Prather et al., 1998). It has been demonstrated that also sediment compaction may significantly increase slope accommodation (Reynolds et al., 1991).

As sediment suspension in turbulent flows depends on bed shear stress, which is directly related to flow velocity, 3D sea floor topography may control sediment deposition, erosion or bypass through flow non-uniformity (Kneller and McCaffrey, 1995). Sea floor bedforms in unconfined settings, normally generated by both erosional or depositional turbidity flows and bottom currents (Rebesco et al., 2014; Symons et al., 2016 and references therein), may

create relative topographic lows (i.e., the convex-up stoss side of the bedform) where the sediment transported by newly generated gravity flows may accumulate. Such lows can be up to 10^2 m height and 10^3 m long, ca. an order of magnitude smaller, in both dimensions, than the intra-slope basins in the Gulf of Mexico, and may act as an intra-slope mini-basin generating what here we call *stoss accommodation*. In the study area, deposition from unconfined flows or bottom currents was probably responsible for the creation of stoss accommodation through the deposition of the large-wavelength bedforms (LB1 to LB4 in Fig. 3; see supplementary material). The ability of a turbidity current to flow across a topographically complex slope, such as a salt withdrawal mini-basin or a large-wavelength bedform, depends on the flow type (surging vs continuous; Lamb et al., 2004), the flow thickness (Lane-Serff et al., 1995), the internal Froude number and the flow stratification (Kneller and McCaffrey, 1999). Complete ponding of the flow occurs if the entire flow is trapped within the topographic depression (Patacci et al., 2015, and references therein), and sedimentation farther downslope is expected after its filling, partial or total, through a process called fill-and-spill (Prather et al., 1998). If the depression is small enough compared to the flow, the turbidity current may be able to surmount its downstream lip: the coarse-grained part of the flow will accumulate within the topographic low while the fine-grained cloud will be able to escape through a process called flow stripping (Piper and Normark, 1983). Experimental results of Lane-Serff et al. (1995) demonstrated that a volume-limited flow (i.e., a surge-like turbidity current) may rise a topographic relief up to 5 times the flow thickness. If we consider the case of one of the largest bedforms discovered so far on the modern sea floor (i.e., the Monterey East channel which shows a maximum wave height of 220 m; Fildani et al., 2006), all the incoming flows thicker than 44 m (with a supercritical regime, as from Lane-Serff et al., 1995) will likely be able to generate overspill from the downstream lip of the bedform. Of course this is an approximation based on Lane-Serff et al. (1995)

numerical results, as flow stratification (density and velocity) is also key in controlling the maximum run-up height of a turbidity current (Kneller and McCaffrey, 1999; Kneller and Buckee, 2000). Considering the example of the Monterey East channel as a conceptual end member, we can argue that turbidity currents thicker than ca. 40 meters will be likely able to overspill from any topographic depressions generated by pre-existing sea floor bedforms. In such scenario, stoss accommodation will be mainly exploited by deposition of the coarser part of the flow, while the fine-grained cloud of the turbidity current will be likely to overspill, potentially creating sandy ponded lobes. This mechanism may affect sediment deposition farther downslope, and the potential development of new sediment corridors. Although with some limitations due to the lack of vertical resolution of the seismic data, this conclusion is supported by the results of this study, which show high RMS amplitude values, considered a proxy for coarse-grained sediment, on the stoss side of each large-wavelength bedform (Fig. 7), and the presence of small channel incisions (named gutter-like channels) along their lee sides, which will control deposition towards the basin. In addition, the short-wavelength bedforms on Lobe A (SB1a, Figs. 3, 5) show crest directions perpendicular to the local slope, probably reflecting deposition from turbidity currents radially spreading at the mouth of channel C-A, on the flat surface generated after the infill of the stoss side of LB1. Similar features have been observed in other context and liked to deposition from turbidity currents (Normandeau et al., 2015). Turbidity currents are highly sensitive to changes in sea floor topography, as divergence or convergence of the streamlines produces sediment deposition or erosion/bypass, respectively (Kneller and McCaffrey, 1995). As in the case of supra-MTD topography (Kneller et al., 2016), pre-existing bedforms may create a complex sea floor topography that will undoubtedly have an effect on the turbidity currents (i.e., deposition, erosion, bypass) depending on the flow properties and direction (see Kneller et al., 2016 for further discussion) with respect to the stoss accommodation space available. Further

work is needed to evaluate the flow behavior across pre-existing large-wavelength bedforms and for turbidity currents unrelated with the deposition of the bedforms themselves, to quantify the facies association of the ponded lobes through direct sediment sampling, and their preservation potential. This may shed lights on defining the role of stoss accommodation in hydrocarbon exploration and in the whole evolution of deep-water depositional systems.

6. Conclusion

Sea floor topography is a first order control on the flow behavior of turbidity currents flowing down the slope of continental margins. Intra-slope basins are normally associated to large-scale deformation of the sea floor, mainly promoted by salt or gravitational tectonics. With an example from the offshore Brazil, here we show that smaller-scale topographic variations of the sea floor associated with bedforms, may have a large effect on subsequent turbidity currents and may promote the formation of coarse-grained ponded lobes. In detail, bedforms characterized by convex-up stoss sides form topographic lows compared to the sea floor near-by, generating stoss accommodation. Depending on the flow characteristics of newly sourced turbidity currents, flow stripping or fill-and-spill may occur, in the first case promoting the formation of sandy ponded lobes. The existence of a 3D topography may capture the coarse-grained fractions of the flows in the relative lows while promoting the delivery of only the fine-grained part downstream. Further studies are needed to understand the role of stoss accommodation in the evolution of turbidity flows and associated deposits, and their preservation potential in the stratigraphy of continental margins.

Acknowledgments

We sincerely thank Petroleum Geo-Services (PGS) and specifically David Hajovsky and Scott Opdyke who kindly provided the dataset and allowed us to show these results. We would also like to thank Schlumberger for providing academic licenses of their software (Petrel), and for their support.

Figure captions

Figure 1

Top: Digital elevation model of the Equatorial Atlantic margin (data from GEBCO). Centre: close-up on the Potiguar Basin in the offshore Brazil; white rectangle represents the full 3D seismic data coverage, while the study area is highlighted in red; black and orange lines mark the position of the bathymetric profiles presented below. Bottom: bathymetric profiles cross the Ceará high and across an open slope setting.

Figure 2

Top: Bathymetric map with 75 m spaced contour lines; white lines oriented NW-SE are the bathymetric profiles presented below, while the thick and continuous red line marks the study area. Note the two large canyon-channel systems bordering the study area (named C-1 and C-3) and the narrower incisional channel C-2. The thin dashed red line marks the slope break at the mouth of incisions C-A and C-B. Bottom: Bathymetric profiles across section AB, CD, EF and GH showing the change of channel depth of C-1, C-2 and C-3 with bathymetric depth; note the position of the slope break in sections AB and CD.

Figure 3

A: Bathymetric map of the study area with 75 m spaced contour lines; the while continuous line marks the position of the bathymetric profile IJ presented in C, while the white dashed lines mark the crest of the large-wavelength bedforms, named LB1 to LB4; the red dashed line marks the slope break at the mouth of C-A and C-B; note the gutter-like channels. B: variance attribute map extracted from the sea floor horizon; note the short-wavelength bedforms (SB1a, SB1b, SB2). C: the bathymetric profile IJ showing the large- and short-wavelength bedforms (gray rectangle) shown in black; the sea floor gradient along the section IJ shown in red, with highlighted the different bedform fields.

Figure 4

Variance attribute extracted from the sea floor and presented in a 3D view. The white dashed lines mark the crest of the large-wavelength bedforms (LB1 to LB4), while the red dashed line marks the slope break at the mouth of C-A and C-B. Note the gutter-like channels (Gc) and the short-wavelength bedform SB2.

Figure 5

Wave length (in km) and wave height (m) of the different bedform fields recognized in this study. The inset is a zoom of the left corner of the diagram to highlight bedforms SB1a, SB1b and SB2.

Figure 6

Plan view of the sea floor slope map (left) and a close-up 3D of the stoss side of LB1 (right); the red dashed line marks the slope break at the mouth of C-A and C-B; blue squares 1 and 2 highlight short-wavelength bedform fields SB1a and SB2 (zoom visible below), while the red square is an example of seismic artefact. Bathymetric profiles across section ab and cd show bedform styles on SB1, while profile ef shows the bedforms on SB2 (bedform's crests pointed by the arrows). Profile gf highlights the seismic artefacts, almost invisible on a bathymetric profile. All the bathymetric profiles are presented at the same scale.

Figure 7

A: Top view of the RMS attribute map extracted from the sea floor horizon; the white dashed lines mark the crest of the large-wavelength bedforms (LB1 to LB4), while the red dashed line marks the slope break. B: RMS amplitude map presented on a 3D view. Note that the stoss side of the bedforms is repeatedly characterized by high RMS amplitude values (named Lobe 1 to Lobe F), while the lee side by lower values. Note the gutter-like channels (Gc). C: Grey-scale version of the RMS attribute map presented in A. This graphic solution is used to better highlight the different features: lobes in orange, crests of the large-wavelength bedforms in dashed white line, slope break in dashed red line.

Figure 8

2D arbitrary lines (see inset map for location) extracted from the 3D seismic cube, all presented at the same scale. Lines 1 to 5 show Lobes A and B, and the internal stratigraphy of the large-wavelength bedform LB1, while Lines 6 and 7 show Lobe D and F, respectively. Horizon H2, highlighted in red (note the truncated reflections in sections 4 and 5, for example), marks the base of bedform LB1. Internal reflections of LB1 are continuous and

low-amplitude (internal erosional surfaces marked by black dashed lines), and present an oblique to upslope direction of migration as seen on the 3D data. Horizon H1, highlighted in black, can be traced at the base of the all the Lobes, which present a positive relief on the sea floor and, when visible, the internal reflections are wavy and high-amplitude. Note the short-wavelength bedform fields on the sea floor reflection. Red dashed lines on seismic Lines 6 and 7 highlight the erosional surface at the base of the LB3 and LB4, in analogy with horizon H2.

Figure 9

Top: Seismic line across the large-wavelength bedforms LB1 to LB4, with highlighted horizon H2 (continuous red line), horizon H1 (black line), and other erosional surfaces (red dashed lines); see trackline in A. Horizon H1 can be traced in much of the study area and forms the base of the ponded Lobes A to F. A: Sea floor bathymetry. B: Structural map of horizon H1. C: Structural map of horizon H2, which highlights the base of LB1. D: Thickness map generated by the difference between the sea floor and horizon H1, which highlights the ponded Lobes A to F. E: Thickness map generated by the difference between H1 and H2 horizons, which highlights the large-wavelength bedform LB1. F: Combined thickness maps showing how Lobe A is confined basinward by LB1, filling the accommodation space generated by the stoss side of LB1.

References

Abreu, V., Sullivan, M., Pirmez, C., Mohrig, D., 2003. Lateral accretion packages (LAPs): an important reservoir element in deep-water sinuous channels. Marine and Petroleum Geology 20, 631-648.

Adeogba, A.A, McHargue, T.R., Graham, S.A., 2005. Transient fan architecture and depositional controls from near-surface 3-D seismic data, Niger delta continental slope. AAPG Bulletin 89, 627-643.

Araripe, P.T., Feijó, F.J., 1994. Carta estratigráfica da Bacia Potiguar. Boletim De Geociências Da Petrobras 8, 127-141.

Armitage, D.A., Romans, B.W., Covault, J.A., Graham, S.A., 2009. The influence of mass-transport-deposit surface topography on the evolution of turbidite architecture: The Sierra Contreras, Tres Pasos Formation (Cretaceous), southern Chile. Journal of Sedimentary Research 79, 287-301.

Badalini, G., Kneller, B., Winker, C.D., 2000. Architecture and processes in the Late Pleistocene Brazos-Trinity turbidite system, Gulf of Mexico Continental Slope. GCSSEPM Foundation 20th Annual Research Conference, Deep-Water Reservoirs of the World, 40-103.

Barton, M.D., 2012. Evolution of an Intra-Slope Apron, Offshore Niger Delta Slope: Impact of Step Geometry on Apron Architecture. In: Prather, B.E., Deptuck, M.E., Mohrig, D., van Hoorn, B., Wynn, R.B., (Eds.), Application of the Principles of Seismic Geomorphology to Continental -Slope and Base-of-Slope Systems: Case Studies from Seafloor and Near-Seafloor Analogues. SEPM Special Publication 99, pp. 181-197.

Beaubouef, R.T., Friedmann, S.J., 2000. High Resolution Seismic/Sequence Stratigraphic Framework for the Evolution of Pleistocene Intra Slope Basins, Western Gulf of Mexico: Depositional Models and Reservoir Analogs. Deep-Water Reservoirs of the World, Gulf Coast SEPM, 40-60.

Berndt, C., Cattaneo, A., Szuman, M., Trincardi, F., Masson, D., 2006. Sedimentary structures offshore Ortona, Adriatic Sea - Deformation or sediment waves? Marine Geology 234, 261-270.

Booth, J.R., Dean, M.C., Duvernay, III, A.E., Styzen, M.J., 2003. Paleo-bathymetric controls on the stratigraphic architecture and reservoir development of confined fans in the Auger Basin: central Gulf of Mexico slope. Marine and Petroleum Geology 20, 563-586.

Brown, A.R., 2004: Interpretation of three-dimensional seismic data, 5th edition. AAPG Memoir 42, Tulsa, Oklahoma, pp. 514.

Casalbore, D., Ridente, D., Bosman, A., Chiocci, F.L., 2017. Depositional and erosional bedforms in Late Pleistocene-Holocene pro-delta deposits of the Gulf of Patti (southern Tyrrhenian margin, Italy). Marine Geology 385, 216-227.

Carter, R.M., 1988. The nature and evolution of deep-sea channel systems. Basin Research 1, 41-54.

Cartigny, M.J.B., Postma, G., van den Berg, J. H., Mastbergen, D.R., 2011. A comparative study of sediment waves and cyclic steps based on geometries, internal structures and numerical modeling. Marine Geology 280, 40-56.

Carvajal, C., Paull, C.K., Caress, D.W., Fildani, A., Lundsten, E., Anderson, K., Maier, K.L., Mcgann, M., Gwiazda, R., Herguera, J.C., 2017. Unraveling the channel-lobe transition zone with high-resolution AUV bathymetry: Navy Fan, Offshore Baja California, Mexico. Journal of Sedimentary Research 87, 1049-1059.

Chen, Q., Sidney, S., 1997. Seismic attribute technology for reservoir forecasting and monitoring. The Leading Edge 16, 445-448.

Condé, V.C., Lana, C.C., Pessoa Neto, O.C., Roesner, E.H., Morais Neto, J.M., Dutra, D.C., 2007. Baciado Ceará. Bol. Geoc. Petrobras 15, 347-355.

Covault, J.A., Kostic, S., Paull, C.K., Ryan, H.F., Fildani, A., 2014. Submarine channel initiation, filling and maintenance from sea-floor geomorphology and morphodynamic modelling of cyclic steps. Sedimentology 61, 1031-1054.

Covault, J.A., Kostic, S., Paull, C.K., Sylvester, Z., Fildani, A., 2017. Cyclic steps and related supercritical bedforms: Building blocks of deep-water depositional systems, western North America. Marine Geology 393, 4-20.

Dalrymple, R.W., Zaitlin, B.A., Boyd, R., 1992. Estuarine facies models: conceptual basis and stratigraphic implications. Journal of Sedimentary Petrology 62, 1130-1146.

Deptuck, M.E., Sylvester, Z., O'Byrne, C.J. Pleistocene seascape evolution above a "simple" stepped slope-western Niger Delta. In: Prather, B.E., Deptuck, M.E., Mohrig, D., van Hoorn, B., Wynn, R.B., (Eds.), Application of the Principles of Seismic Geomorphology to Continental -Slope and Base-of-Slope Systems: Case Studies from Seafloor and Near-Seafloor Analogues. SEPM Special Publication 99, pp. 199-222.

Ferry, J.N., Mulder, T., Parize, O., Raillard, S., 2005. Concept of equilibrium profile in deep-water turbidite system: effects of local physiographic changes on the nature of sedimentary process and the geometries of deposits. In: Hodgson, D.M., Flint, S.S., (Eds.), Submarine Slope Systems: Processes and Products, Geological Society of London, Special Publications 244, pp. 181-193.

Fildani, A., Normark, W.R., Kostic, S., Parker, G., 2006. Channel formation by flow stripping: large-scale scour features along the Monterey East Channel and their relation to sediment waves. Sedimentology 53, 1265-1287.

Fildani, A., Hubbard, S.M., Covault, J.A., Maier, K.L., Romans, B.W., Traer, M., Rowland, J.C., 2013. Erosion at inception of deep-sea channels. Marine and Petroleum Geology 41, 48-61.

Hawie, N., Covault, J.A., Dunlap, D., Sylvester, Z., 2018. Slope-fan depositional architecture from high-resolution forward stratigraphic models. Marine and Petroleum Geology 91, 576-585.

Heiniö, P., Davies, R.J., 2007. Knickpoint migration in submarine channels in response to fold growth, western Niger Delta. Marine and Petroleum Geology 24, 434-449.

Hughes Clarke, J.E., 2016. First wide-angle view of channelized turbidity currents links migrating cyclic steps to flow characteristics. Nature Communications 7, 1-13.

Jervey, MT., 1988. Quantitative geological modeling of siliciclastic rock sequences and their seismic expression. In: Wilgus, C.K., Hasting, B.S., Kendall, C.G.S.C., Posamentier, H.W., Ross, C.A., Van Wagoner, J., (Eds.), Sea-level Changes-an Integrated Approach, 42, SEPM Special Publication, pp. 47-69.

Jobe, Z.R., Sylvester, Z., Parker, A.O., Howes, N., Slowey, N., Pirmez, C., 2015. Rapid adjustment of submarine channel architecture to changes in sediment supply. Journal of Sedimentary Research 85, 729-753.

Jobe, Z.R., Sylvester, Z., Howes, N., Pirmez, C., Parker, A.O., Cantelli, A., 2017. High-resolution, millennial-scale patterns of bed compensation on a sand-rich intraslope submarine fan, western Niger Delta slope. Geol. Soc. Am. Bull. 129, 23-37.

Jovane, L., Figueiredo, J.J.P., Alves, D.V.P., Iacopini, D., Giorgioni, M., Vannucchi, P., Moura, D.S., Bezerra, F.H.R., Vital, H., Rios, I.L.A., Molina, E.C., 2016. Seismostratigraphy of the Ceará Plateau: Clues to Decipher the Cenozoic Evolution of Brazilian Equatorial Margin. Frontiers in Earth Science doi:10.3389/feart.2016.00090.

Kneller, B., McCaffrey, W.D., 1995. Modelling the effects of salt-induced topography on deposition from turbidity currents. GCSSEPM Foundation 16th Annual Research Conference Salt, Sediment and Hydrocarbons, 137-145.

Kneller, B., McCaffrey, W.D., 1999. Depositional effects of flow nonuniformity and stratification within turbidity currents approaching a bounding slope: deflection, reflection, and facies variation. Journal of Sedimentary Research 69, 980-991.

Kneller, B., Buckee, C., 2000. The structure and fluid mechanics of turbidity currents: a review of some recent studies and their geological implications. Sedimentology, 47, 62-94.

Kneller, B., 2003. The influence of flow parameters on turbidite slope channel architecture. Marine and Petroleum Geology 20, 901-910.

Kneller, B., Dykstra, M., Fairweather, L., Milana, J.P., 2016. Mass-transport and slope accommodation: Implications for turbidite sandstone reservoirs. AAPG Bulletin 100, 213-235.

Kolla, V., Bandyopadhyay, A., Gupta, P., Mukherjee, B., Ramana, D.V., 2012. Morphology and internal structure of a recent upper Bengal fan-valley complex. In: Prather, B.E., Deptuck, M.E., Mohrig, D., Van Horn, B., Wynn, R.B., (Eds.), Application of the Principles of Seismic Geomorphology to Continental-Slope and Base-of-Slope Systems: Case Studies from Seafloor and Near-Seafloor Analogues, SEPM, Special Publication 99, pp. 347-369.

Lamb, M.P., Hickson, J.G., Marr, B., Sheets, B., Paola, C., Parker, G., 2004. Surging and continuous turbidity currents: Flow dynamics and deposits in an experimental intraslope minibasin. Journal of Sedimentary Research 74, 148-155.

Lane-Serff, G.F., Beal, L.M., Hadfield, T.D., 1995. Gravity current flow over obstacles. Journal of Fluid Mechanics 292, 39-53.

Matos, R.M.D., 2000. Tectonic evolution of the Equatorial South Atlantic. In: Mohriak, W.U., Talwani, M.. (Eds.), Atlantic Rifts and continental margins, Geophysical Monograph, 115, Amreican Geophysical Union, pp. 332-354.

Mutti, E., Tinterri, R., Remacha, E., Mavilla, N., Angella, S., Fava, L., 1999. An introduction to the analysis of ancient turbidite basins from an outcrop perspective AAPG Course Note 39, pp. 93.

Normandeau, A., Lajeunesse, P., St-Onge, G., 2015. Submarine canyons and channels in the Lower St. Lawrence Estuary (Eastern Canada): Morphology, classification and recent sediment dynamics. Geomorphology 241, 1-18.

Normandeau, A., Lajeunesse, P., Poiré, A.G., Francus, P., 2016. Morphological expression of bedforms formed by supercritical sediment density flows on four fjord-lake deltas of the south-eastern Canadian Shield (Eastern Canada). Sedimentology 63, 2106-2129.

Normark, W.R., Piper, D.J.W., Posamentier, H., Pirmez, C., Migeon, S., 2002. Variability in form and growth of sediment waves on turbidite channel levees. Marine Geology 192, 23-58.

Paull, C.K., Ussler III, W., Caress, D.W., Lundsten, E., Covault, J.A., Maier, K.L., Xu, J. and Augenstein, S., 2010. Origins of large crescent-shaped bedforms within the axial channel of Monterey Canyon, offshore California. Geosphere 6, 755-774.

Paull, C.K., Caress, D.W., Ussler III, W., Lundsten, E., Meiner-Johnson, M., 2011. High-resolution bathymetry of the axial channels within Monterey and Soquel submarine canyons, offshore central California. Geophere 7, 1077-1101.

Patacci, M., Haughton, P.D.W., McCaffrey, W.D., 2015. Flow behavior of ponded turbidity currents. Journal of Sedimentary Research 85, 885-902.

Piper, D.J.W., Normark, W.R., 1983. Turbidite depositional patterns and flow characteristics, Navy submarine fan, California Borderland. Sedimentology 30, 681-694.

Piper, D.J.W., Normark, W.R., 2009. Processes that initiate turbidity currents and their influence on turbidites: a marine geology perspective. Journal of Sedimentary Research 79, 347-362.

Pirmez, C., Beauboeuf, R.T., Friedmann, S.J., Mohrig, D.C., 2000. Equilibrium profile and baselevel in submarine channels: examples from Late Pleistocene systems and implications for the architecture of deepwater reservoirs. In: Weimer, P., Slatt, R.M., Coleman, J., Rosen, N.C., Nelson, H., Bouma, A.H., Styzen, M.J., Lawrence, D.T., (Eds.), Deep water reservoirs of the world, GCSSEPM Foundation, Houston (2000), pp. 782-805.

Prather, B.E., Booth, J.E., Steffens, G.S., Craig, P.A., 1998. Classification, lithologic calibration, and stratigraphic succession of seismic facies of intraslope basins, deep-water Gulf of Mexico. American Association of Petroleum Geologists Bulletin 82, 701-728.

Prather, B.E., 2003. Controls on reservoir distribution, architecture and stratigraphic trapping in slope settings. Marine and Petroleum Geology 20, 529-545.

Prather, B.E., Pirmez, C., Winker, C.D. 2012. Stratigraphy of linked intraslope basins: Brazos-Trinity system Western Gulf of Mexico. In: Prather, B.E., Deptuck, M.E., Mohrig, D., van Hoorn, B., Wynn, R.B. (Eds.), Application of the Principles of Seismic Geomorphology to Continental -Slope and Base-of-Slope Systems: Case

Studies from Seafloor and Near-Seafloor Analogues. SEPM Special Publication 99, pp. 83-109.

Rebesco, M., Hernández-Molina, F.J., van Rooij, D., Wåhlin, A., 2014. Contourites and associates sediments controlled by deep-water circulation processes: State of the art and future considerations. Marine Geology 352, 111-154.

Reijenstein, H.M., Posamentier, H.W., Bhattacharya, J.P., 2011. Seismic geomorphology and high-resolution seismic stratigraphy of inner-shelf fluvial, estuarine, deltaic, and marine sequences, Gulf of Thailand. AAPG Bulletin 95, 1959-1990.

Rijks, E.J.H., Jauffred, J.C.E.M., 1991. Seismic interpretation 29; attribute extraction; an important application in any detailed 3-D interpretation study. The Leading Edge 10, 11-19.

Reynolds, D.J., Steckler, M.S., Coakley, B.J., 1991. The role of the sediment load in sequence stratigraphy: The influence of flexural isostasy and compaction. Journal of Geophysical Research B01914.

Sinclair, H.D., Tomasso, M., 2002. Depositional Evolution of Confined Turbidite Basins. Journal of Sedimentary Research 72, 451-456.

Smith, R., 2004. Silled sub-basins to connected tortuous corridors: sediment distribution systems on topographically complex sub-aqueous slopes. Geological Society of London Special Publications 222, 23-43.

Smith, D.P., Kvitek, R., Iampietro, P.J., Wong, K., 2007. Twenty-nine months of geomorphic change in upper Monterey Canyon (2002–2005). Marine Geology 236, 79-94.

Soutter, E.L., Kane, I.A., Huuse, M., 2018. Giant submarine landslide triggered by Paleocene mantle plume activity in the North Atlantic. Geology 46, 511-514.

Symons, W.O., Sumner, E.J., Talling, P.J., Cartigny, M.J.B., Clare, M.A., 2016. Large-scale sediment waves and scours on the modern seafloor and their implications for the prevalence of supercritical flows. Marine Geology 371, 130-148.

Talling, P.J., Allin, J., Armitage, D.A., Arnott, R.W.C., Cartigny, M.J.B., Clare, M.A., Felletti, F., Covault, J.A., Girardclos, S., Hansen, E., Hill, P.R., Hiscott, R.N., Hogg, A.J., Hughes Clarke, J.E., Jobe, Z.R., Malgesini, G., Mozzato, A., Naruse, H., Parkinson, S., Peel, F.J., Piper, D.J.W., Pop, E., Postma, G., Rowley, P., Sguazzini, A., Stevenson, C.J., Sumner, E.J., Sylvester, Z., Watts, C., Xu, J., 2015. Key future directions for research on turbidity currents and their deposits. Journal Sedimentary Research 85, 153-169.

Vail, PR., 1987. Seismic stratigraphy interpretation using sequence stratigraphy. Part I: Seismic stratigraphy interpretation procedure. In Atlas of Seismic Stratigraphy, ed. AW Bally, pp. 1-10. Am. Assoc. Petrol. Geol. Stud. Geol. No. 27, Vol. 1. 125 pp.

Winker, C.D., 1996. High-resolution seismic stratigraphy of a late Pleistocene submarine fan ponded by salt-withdrawal mini-basins on the Gulf of Mexico continental slope. 28th Annual Offshore Technology Conference, Proceedings, pp. 619-628.

Wynn, R.B., Stow, D.A.V., 2002. Classification and characterisation of deep-water sediment waves. Marine Geology 192, 7-22.

Figure 1

Click here to download high resolution image

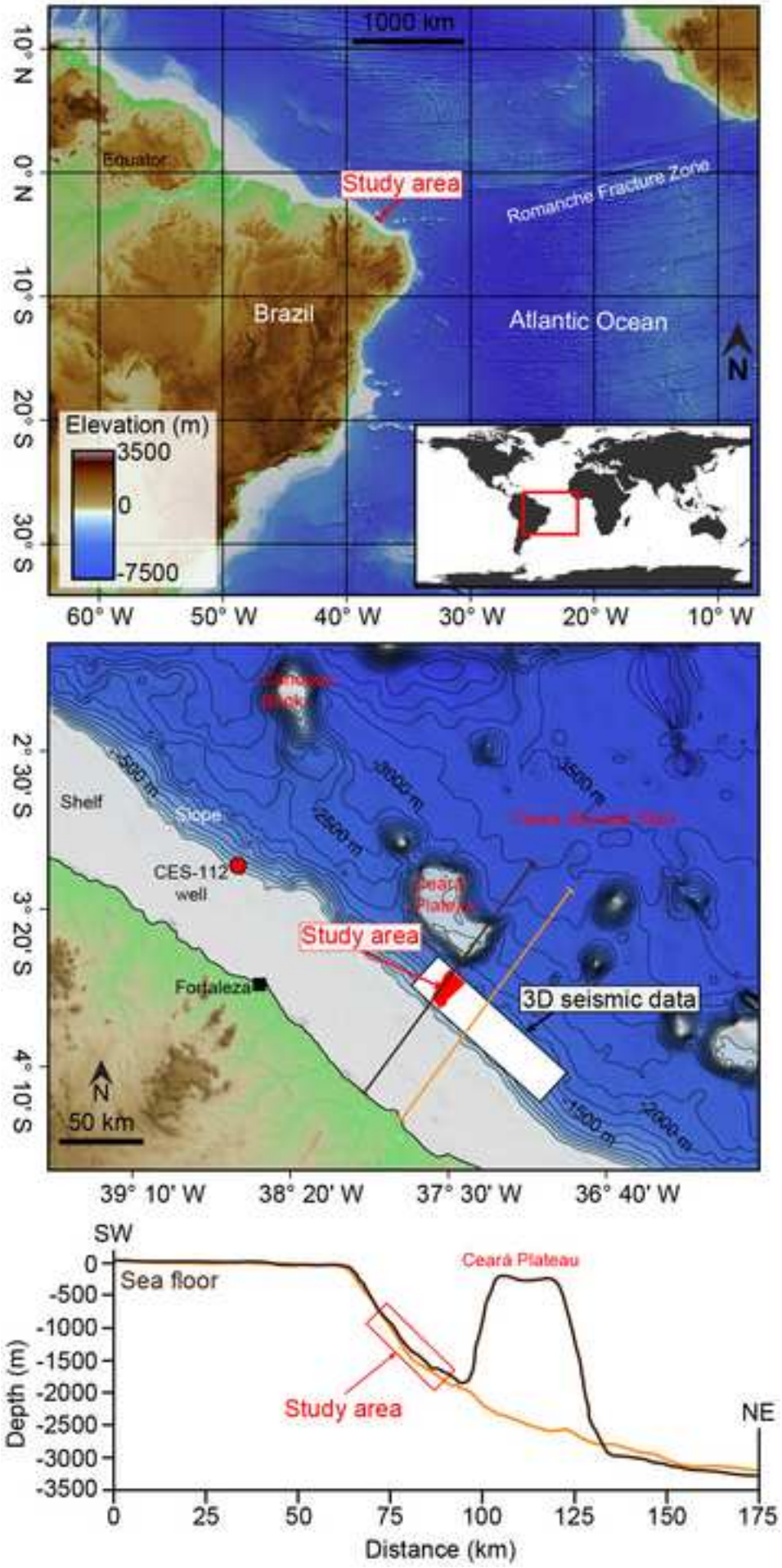

Figure 2

Click here to download high resolution image

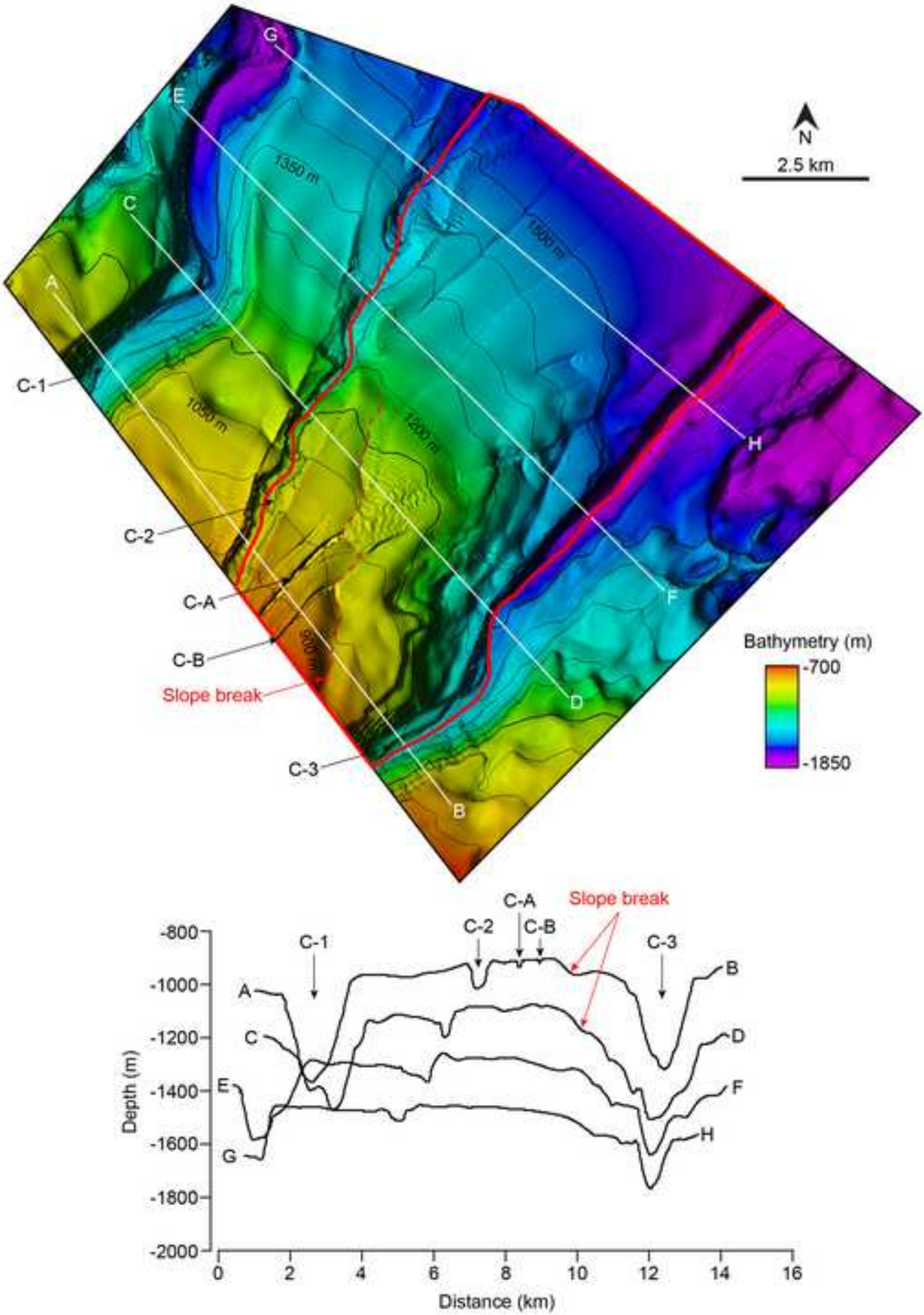

Figure 3

Click here to download high resolution image

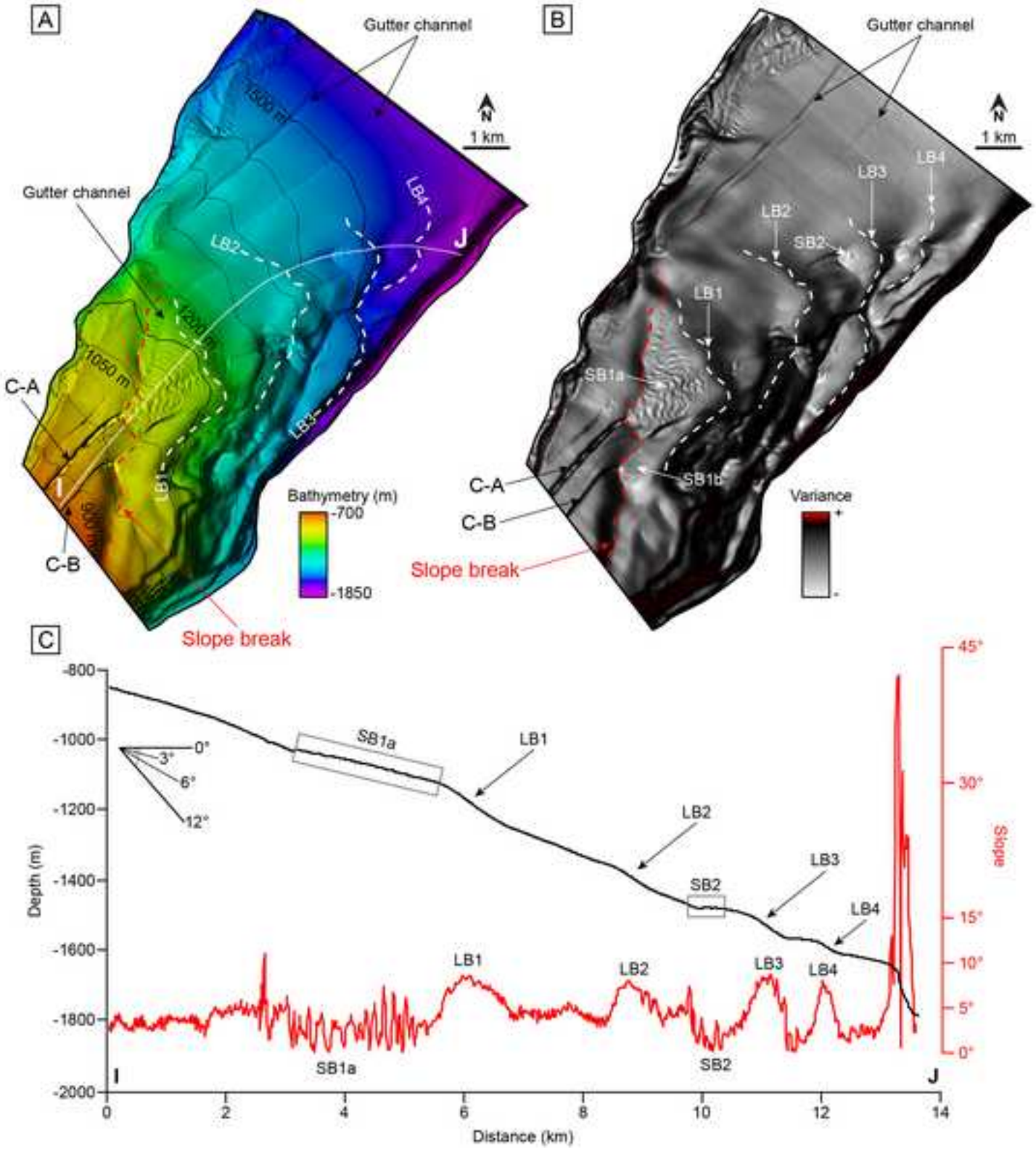

Figure 4

Click here to download high resolution image

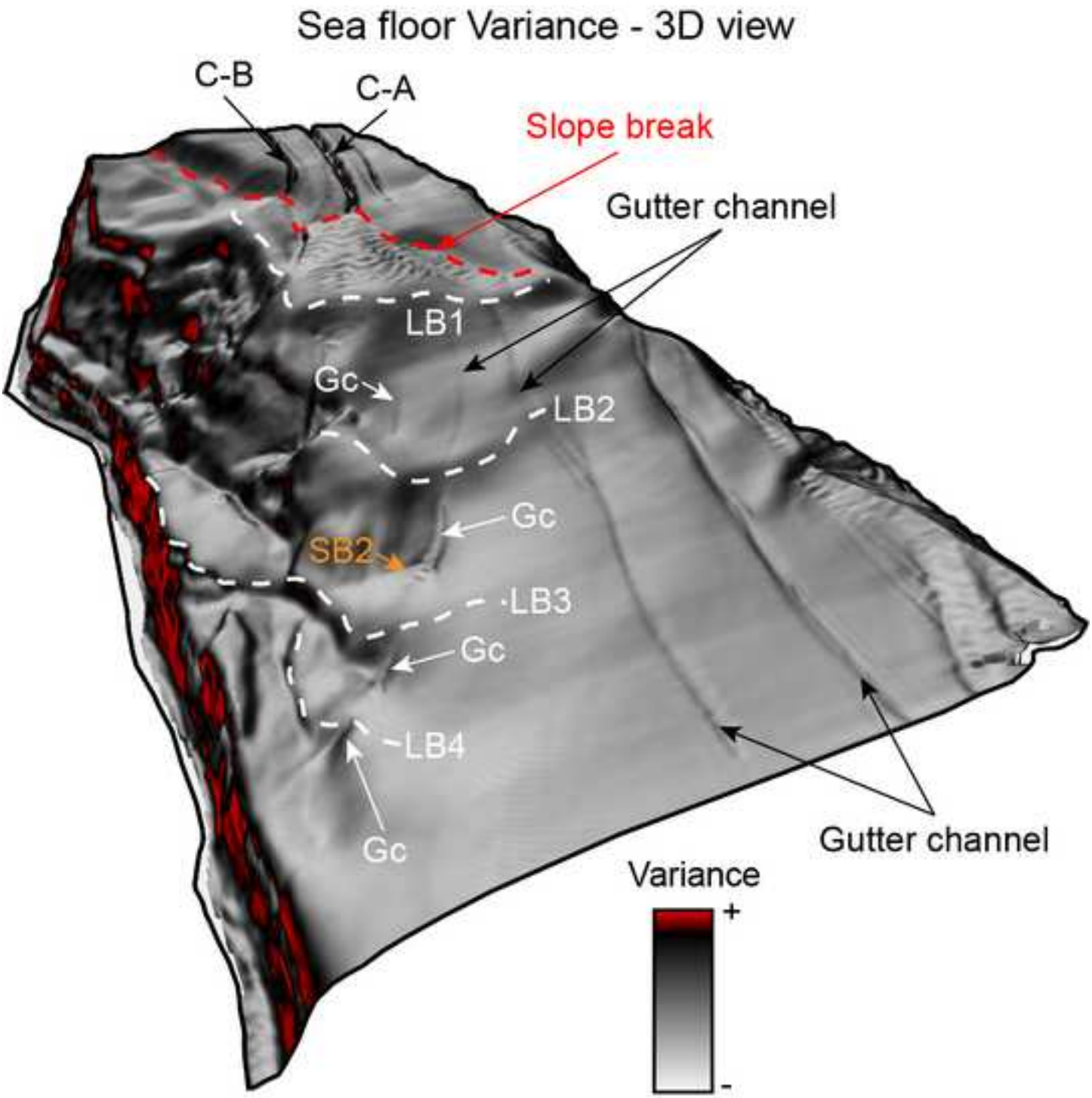

Figure 5

Click here to download high resolution image

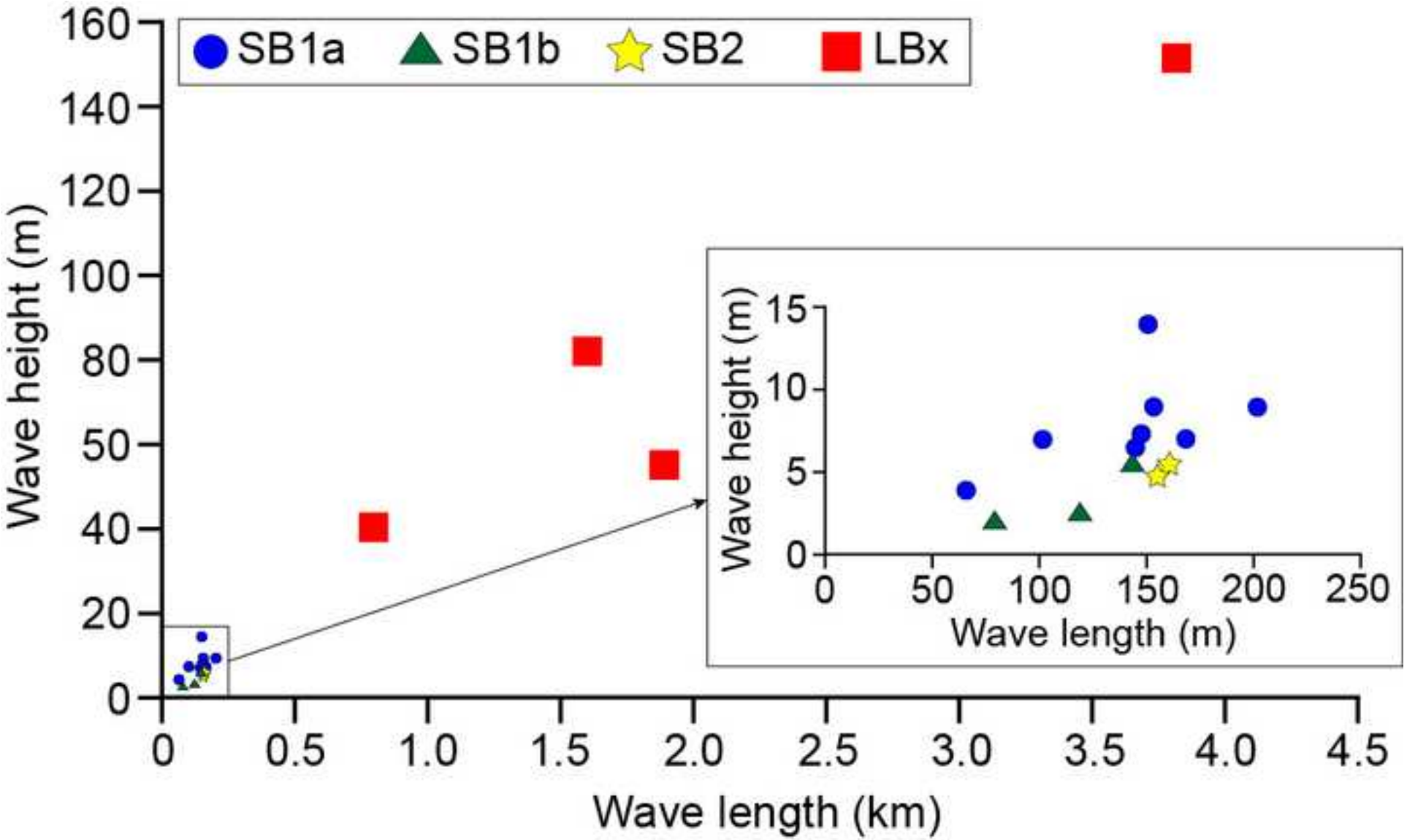

Figure 6

Click here to download high resolution image

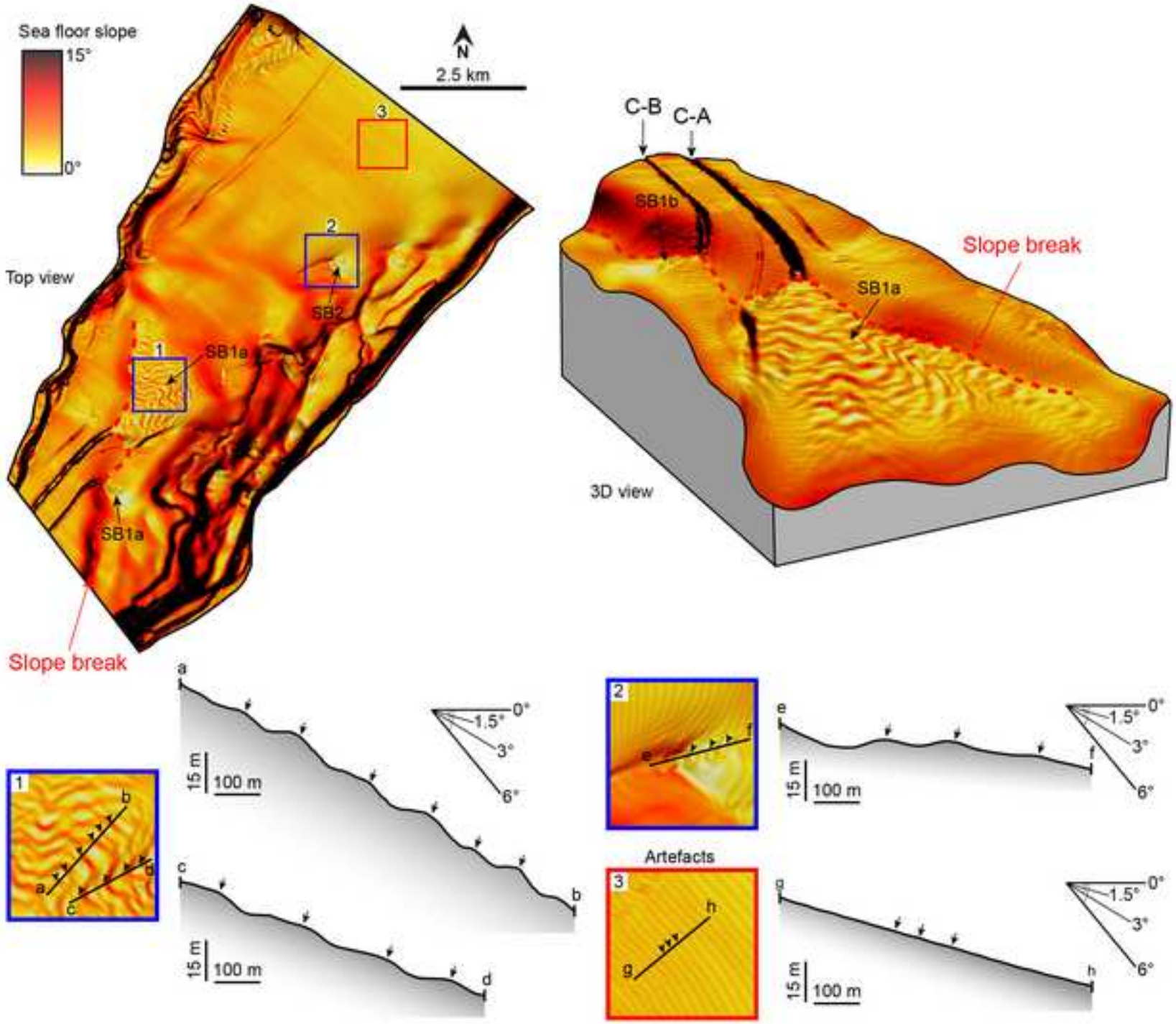

Figure 7

Click here to download high resolution image

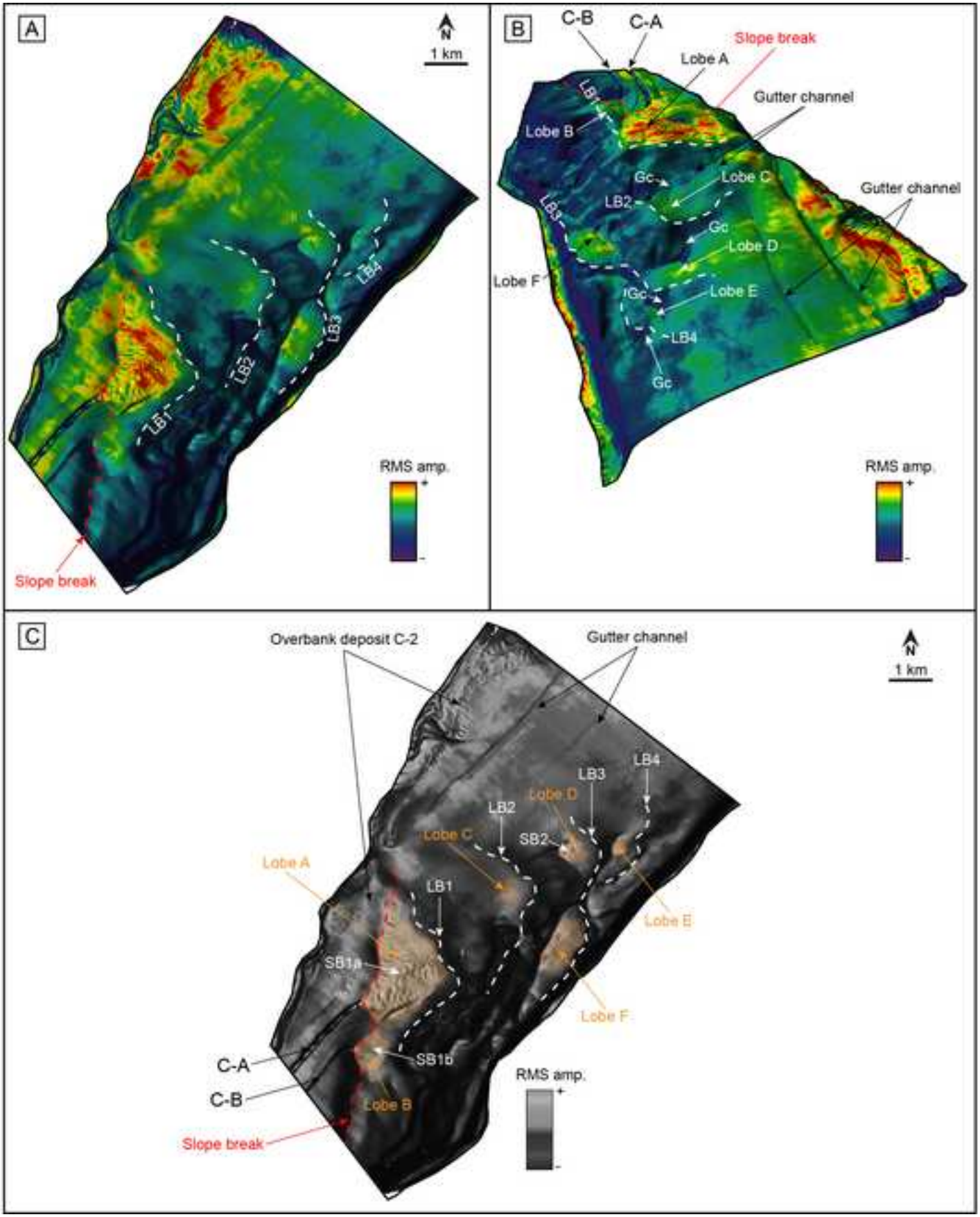

Figure 8

Click here to download high resolution image

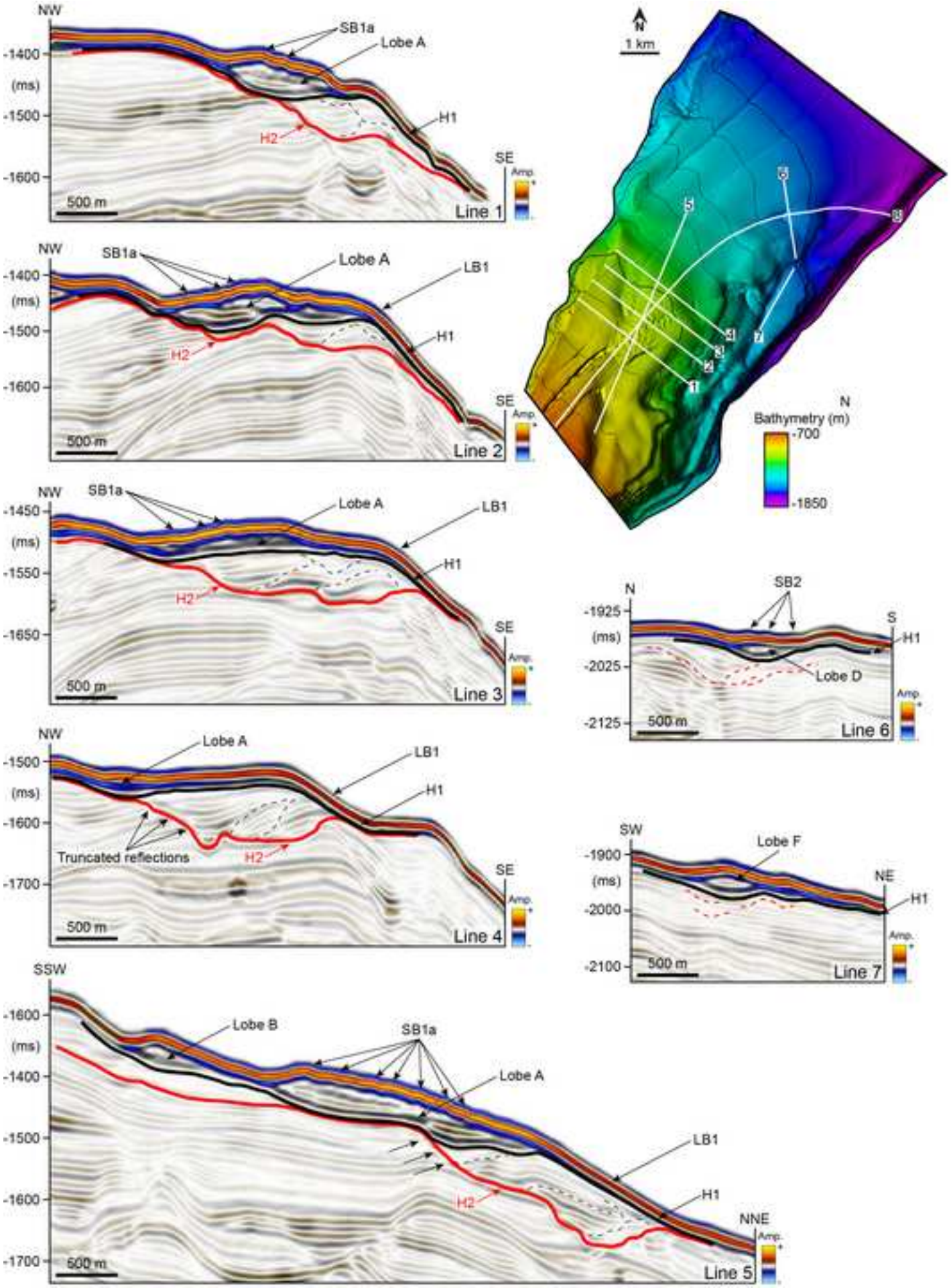

Figure 9

Click here to download high resolution image